Chapter 3. High-Frequency (>100 GHz) and High-Speed (<1 ps) Electronic Devices

Academic and Research Staff

Professor Qing Hu, Dr. Gerhard de Lange, Dr. Simon Verghese

Visiting Scientists and Research Affiliates

Dr. Thomas Schäpers

Graduate Students

James Ernstmeyer, Brian R. Jacobson, Ilya Lyubomirsky, Arifur Rahman, Farhan Rana, Rolf A. Wyss, Bin Xu, Noah D. Zamdmer

3.1 Introduction

Millimeter wave and far-infrared frequencies (f > 100 GHz) remain one of the most underdeveloped frequency ranges, even though there are a great number of potential applications in remote sensing, spectroscopy, plasma diagnostics, and communications. This is because the millimeter wave and far-infrared frequency range falls between two other frequency ranges in which conventional semiconductor devices are usually operated, the microwave frequency range and the near-infrared and optical frequency range. Semiconductor devices which utilize the classical diffusive transport of electrons, such as diodes and transistors, have a high frequency limit. This limit is set by the time electrons take to travel a certain distance. Currently, electron mobility and the smallest feature size which can be fabricated by lithography limit the frequency range to below several hundred GHz. Semiconductor devices based on quantum mechanical interband transitions, however, are limited to frequencies higher than those corresponding to the semiconductor energy gap, which is higher than 10 THz for most bulk semiconductors. Therefore, a large gap exists from 100 GHz to 10 THz in which very few devices are available.

Semiconductor quantum-effect devices (which can be loosely termed "artificial atoms"), including both vertically grown quantum-well structures and laterally confined mesoscopic devices, are human-made quantum mechanical systems in which the energy levels can be chosen by changing the size of the device. Typically, the frequency corresponding to the intersubband transitions is in the millimeter-wave to THz range ($\Delta E \sim 1$-4 meV) for the lateral quantum-effective devices, and above one THz for the vertical quantum wells. It is therefore appealing to develop ultrahigh-frequency devices, such as radiation detectors and mixers, and THz lasers utilizing the intersubband transitions in these devices. Furthermore, the study of the interaction between photons (with energies comparable to the intersubband spacings) and the quantum-effect devices (artificial atoms) is analogous to optical spectroscopy in atomic physics. Naturally, this study will literally shine "new light" on these novel devices and new information will be obtained that could not be extracted from dc transport measurements. It is also clear that devices with THz characteristic frequencies will have picosecond speed response. Such ultrahigh-speed devices could be useful in easing the electronic "bottleneck" in the current fiber optical communication systems, in which only a small fraction of the 20-THz bandwidth of optical fibers are utilized because of the slow speed of electronic devices.

In addition to new physical concepts, novel technologies must also be developed to meet the challenges at these high frequencies. Conventional mechanically machined horn antennas integrated with waveguide cavities have been the workhorse at microwave and millimeter-wave frequencies since they were first implemented more than 50 years ago during World War II. Very high antenna gain and essentially perfect antenna efficiency can be achieved using these structures. However, they are expensive, bulky, and incompatible with arrays. In order to overcome these problems, there have been new developments in micromachining to fabricate the horn antenna structures. In these structures, the active elements and their planar antennas are fabricated on a free-standing thin (~ 1 micron) SiN membrane, which is suspended over a silicon pyramidal horn that is formed by anisotropic etching, or micromachining. The side walls of this micromachined structure can then be coated with Au to form a horn antenna. Compared to conventional waveguide horn antennas, this novel micromachined structure has several major advantages. It is easier

to fabricate fine three-dimensional structures by using photolithography. Horn antennas with micron precision can be easily defined and inexpensively mass produced. It is made on Si or GaAs wafers and compatible with thin-film technology. Thus, active elements, such as RF and IF amplifiers, mixers and video detectors, local oscillators, and post-detection signal processors, can be integrated monolithically with the antenna structures to form monolithic transmitter/receiver systems. It is lightweight and compact. The most attractive feature of the micromachined structure is that focal-plane arrays can be fabricated easily on a single wafer, as illustrated in figure 1b. Such systems will yield a significantly improved spatial resolution in remote sensing, and a much greater antenna gain when implemented with phased-arrays.

In our group, we are systematically investigating physical and engineering issues that are relevant to high-frequency and high-speed devices. Specifically, we are working on micromachined millimeter- and submillimeter-wave devices, far-infrared and picosecond time-resolved transport studies of lateral quantum-effect devices, and development of far-infrared lasers, photodetectors, and optical parametric amplifiers using multiple quantum-well structures.

3.2 Micromachined Millimeter-wave Devices

Sponsors

Advanced Research Projects Agency
Contract MDA972-90-C-0021
National Aeronautics and Space Administration
Grant NAG2-693
Contract 959705

Project Staff

Gerthard de Lange, Brian R. Jacobson, Arifur Rahman, Professor Qing Hu, in collaboration with Dr. Rich Ralston and Group 86 at MIT Lincoln Laboratory

3.2.1 Micromachined Millimeter-wave SIS Receivers

SIS (superconductor-insulator-superconductor) heterodyne receivers have been demonstrated to be the most sensitive receivers throughout 30-840 GHz frequency range. The challenge now in the SIS receiver technology is to extend their operating frequency into the THz range and to develop focal-plane arrays in order to improve the efficiency of data acquisition. To achieve these goals, we are currently developing a novel scheme to couple the millimeter-wave and infrared signals to the superconducting devices by using a micromachined horn antenna and a planar antenna supported by a thin (~ 1 micron) membrane, as shown in figure 1a. As stated in the introduction, this novel micromachined antenna structure can be produced with a high precision using photolithography, and it can be utilized in focal-plane arrays, as shown in figure 1b.

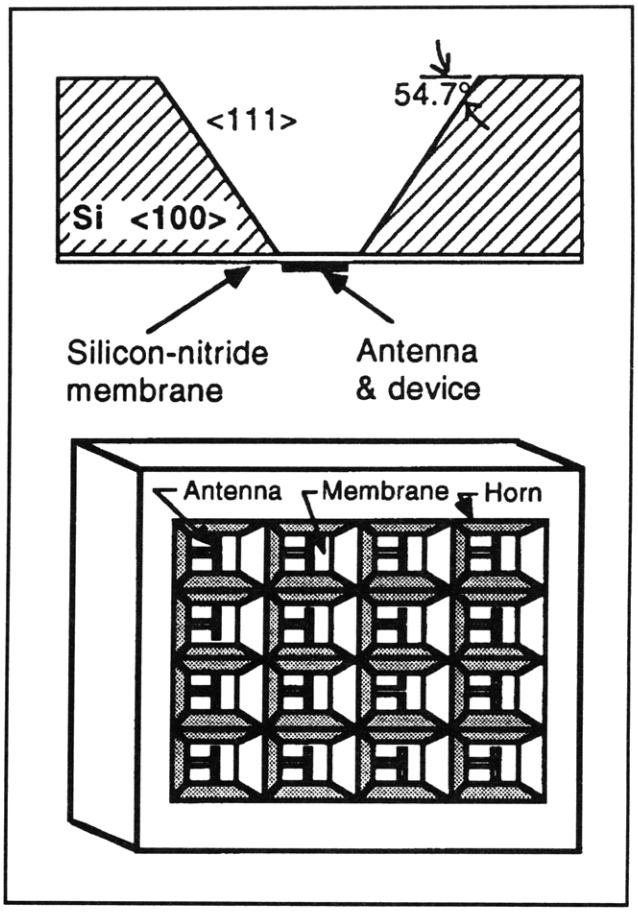

Figure 1. (a) Example of a micromachined horn antenna structure that is made by anisotropically etching a <100> silicon wafer; (b) Schematic of a focal-plane array on a single wafer made using micromachining.

Following our initial success in fabricating high-quality high-current-density SIS junctions on free-standing SiN membranes, we have further improved our micromachining techniques for whole-wafer fabrication, higher yield, and better quality side walls that are critical for the antenna performance. Recently, we have constructed and tested a W-band (75-110 GHz) micromachined SIS receiver. Figure 2 shows the pumped and unpumped I-V characteristics of an SIS receiver in a micromachined antenna structure. It also shows the response to a hot (the curved marked as 300 K)

and a cold (at 77 K) blackbody radiator at the intermediate frequency (IF). The 4-dB difference between the two curves corresponds to a double-sideband (DSB) receiver noise temperature of 70 K (without any corrections). By using SIS junctions with higher current densities or by using integrated tuning elements to tune out the junction capacitance at the operating frequencies, we are confident that we can reduce the noise temperature by at least another factor of two, which will be comparable to the best results achieved from conventional waveguide SIS receivers.

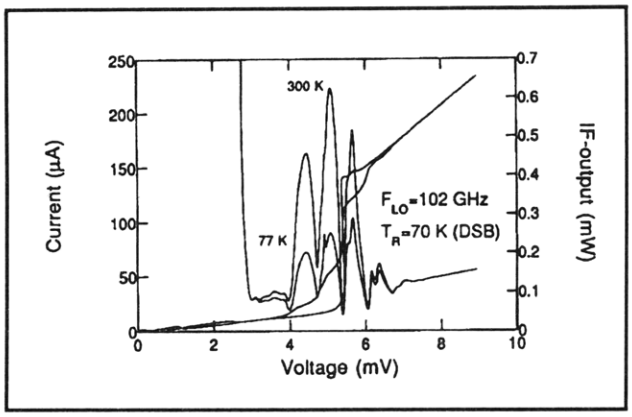

Figure 2. Pumped and unpumped I-V characteristics of an SIS device in a micromachined antenna structure. The curve marked 300 K corresponds to the IF response when a hot (300 K) blackbody radiator is placed in front of the receiver, while the curve marked 77 K is with a cold load.

We have measured the mixer performance over the whole W-band (75-110 GHz). The lowest noise temperature occurs at 102 GHz (the system was designed for 95 GHz), and the 3-dB bandwidth is approximately 15 percent, which is comparable to those of fix-tuned waveguide receivers. This achievement has given us confidence that the micromachined antenna structure is a competitive alternative to the conventional waveguide systems.

3.2.2 Micromachined Room-temperature Millimeter-wave Sensors

Due to a millimeter-wave's (especially around the 94-GHz atmospheric window) great penetration in foggy, dusty, and smoky environments, and to its much better spatial resolutions compared to the longer wavelengths at microwave frequencies, sensitive room-temperature millimeter-wave devices are very useful in imaging and object identification and tracking. They are important for both military and commercial applications, such as motor vehicle collision avoidance radars. Based on our recent remarkable success in the development of micromachined SIS receivers, we are currently developing the most sensitive room-temperature millimeter-wave sensors using the micromachining technology.

We plan to use microbolometers (whose dimension is approximately several microns, as shown in figure 3) in our micromachined systems. Microbolometers are easy to make (in fact, they are much easier to make than the superconducting tunnel junctions in our current systems), robust, and sensitive. In addition, our micromachined millimeter-wave structure is ideal for bolometric detectors in such a way that the thin SiN membrane provides a natural thermal isolation that a sensitive bolometer requires.

The dominating noise source in bolometric detectors is the 1/f noise associate with the resistive element (which is usually made out of semimetal materials, such as Bi, to achieve a high resistance value for impedance matching). Recently, it was discovered in the field of superconducting electronics that a commonly used superconducting material, Nb, has an order of magnitude lower level of 1/f noise (at room-temperature) than Bi while still provides sufficiently high resistivity for impedance matching. Assume we operate the microbolometers above the 1/f noise frequency region and use low-noise on-chip amplifiers, the NEP (noise equivalent power) of the microbolometers is limited by the temperature fluctuation, i.e., the phonon noise. Using realistic parameters for thermal conductance, a room-temperature Nb microbolometer can achieve an NEP of 6×10^{12} W/(Hz)$^{1/2}$. This is more than one order of magnitude lower than that of pyroelectric detectors, which are the commonly used room-temperature millimeter-wave sensors. This level of reduction in NEP will significantly improve the sensitivity of the detectors and reduce the required integration time by at least a factor of one hundred for the same signal/noise ratio.

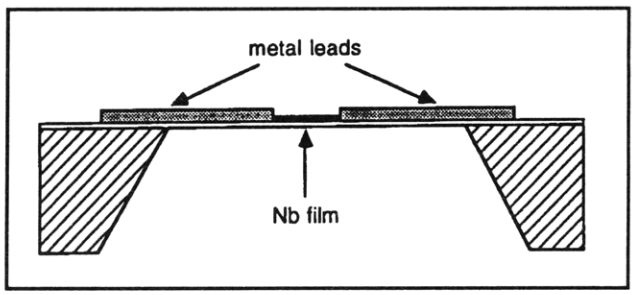

Figure 3. Schematic of a microbolometer supported by a thin membrane, which provides a good thermal insulation.

3.3 Far-infrared and Picosecond Time-resolved Transport Studies of Quantum-effect Devices

3.3.1 Far-infrared Studies of Antenna-coupled Quantum Point Contacts

Sponsor

National Science Foundation/MRSEC
Grant DMR 94-00334

Project Staff

Rolf A. Wyss, Professor Qing Hu, in collaboration with Professor Jesús A. del Alamo, Dr. Michael R. Melloch,[1] Michael J. Rooks[2]

Quantum transport has been one of the most active fields in solid-state physics in recent years. Advances in material preparation have made quantum phenomena profound in electron transport for many semiconductor quantum devices such as quantum point contacts, quantum dots, quantum wires, quantum wells, superlattices, etc. In clean samples and at low temperatures, electrons can travel through the whole sample without suffering phase-destructive scattering. Extensive work has been done to study various features of such phase-coherent quantum transport. However, most of the experiments reported so far are limited to dc transport measurements and far-infrared spectroscopy measurements.

It is well known in the field of superconducting tunneling that photons can assist the tunneling process, provided the tunneling is elastic. In a broad sense, elastic tunneling is a phase-coherent quantum transport process in a classically forbidden region. Therefore, all the results of photon-assisted tunneling can be applied to the study of photon-assisted quantum transport in semiconductor devices. This will provide a new dimension to study the exciting quantum transport phenomena. Novel long-wavelength optoelectronic devices may also emerge from this research.

In this project, we intend to study the interaction between far-infrared photons and ballistic electrons in quantum point contact devices, whose schematic is shown in figure 4a.

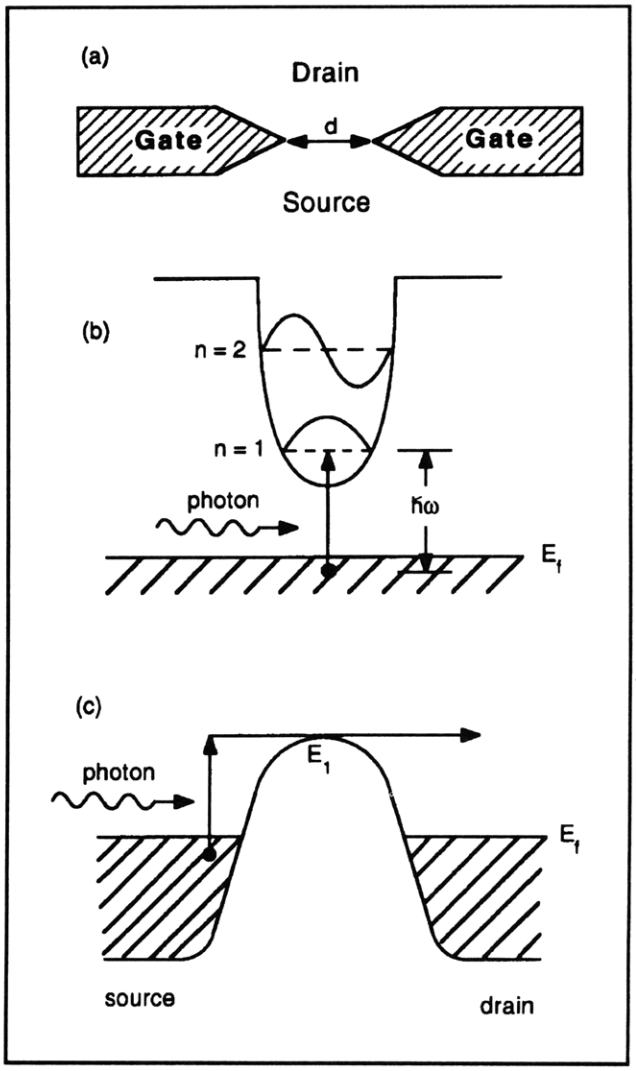

Figure 4. (a) Schematic of a quantum point contact. (b) and (c) Illustration of photon-assisted over-the-barrier quantum transport.

We have fabricated several antenna-coupled quantum point contact devices using a combination of optical and electron-beam lithography. The dc transport measurement of the drain/source transport showed high quality of the devices. Under coherent far-infrared radiation at 285 GHz, a pronounced photon-induced drain/source current is produced throughout the gate voltage range in which the device exhibits the behavior of a one-dimensional electron system. This photon-induced current is attributed to a bolometric effect as described in the previous report.

---

[1] Purdue University, West Lafayette, Indiana.

[2] Cornell National Nanofabrication Facility, Ithaca, New York.

In addition to the photoconductive effect, we have recently discovered a pronounced photovoltaic effect in several antenna-coupled quantum point contacts irradiated from 280 GHz to 2.5 THz. Figure 5a shows the drain/source current of an irradiated quantum point contact without external drain/source bias. This induced current tracks the subband structure in a very regular manner that is similar to the transconductance of the device measured without radiation. We have identified this photovoltaic effect as a result of thermopower due to an asymmetric heating of the source and drain. This analysis is supported by an experimental evidence that by shifting the focal spot of the radiation, we can reverse the polarity of the photon-induced current, as shown in figure 5b.

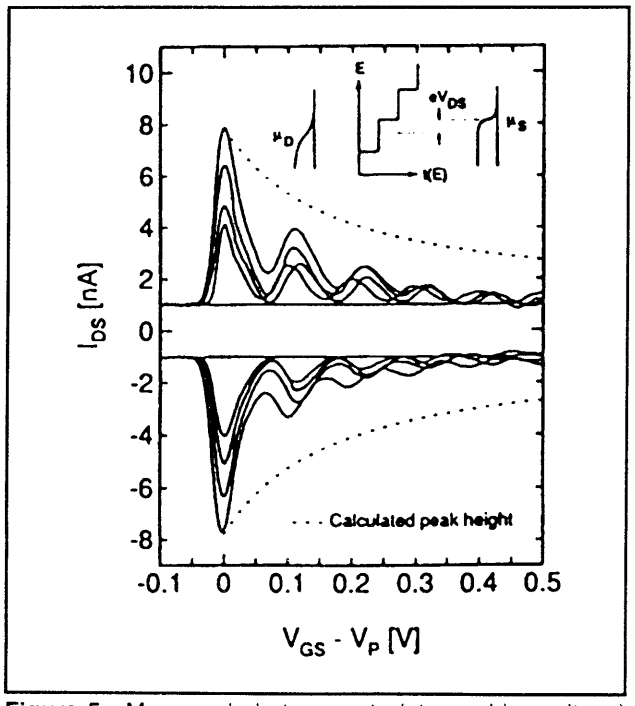

Figure 5. Measured photocurrents (at zero bias voltage) at different radiation power levels. (a) Positive currents correspond to beaming toward the source region, while (b) negative currents correspond to beaming toward the drain region.

By comparing the measured thermopower signals with theoretical predictions based on ballistic transport in one-dimensional systems, we have discovered that it is essential to include the electronic thermal conductance between the source and drain in order to account for the rapid decrease of the thermopower signals at higher subbands. The measured and calculated results (including this thermal conductance) are plotted in figure 6, which shows an excellent agreement.

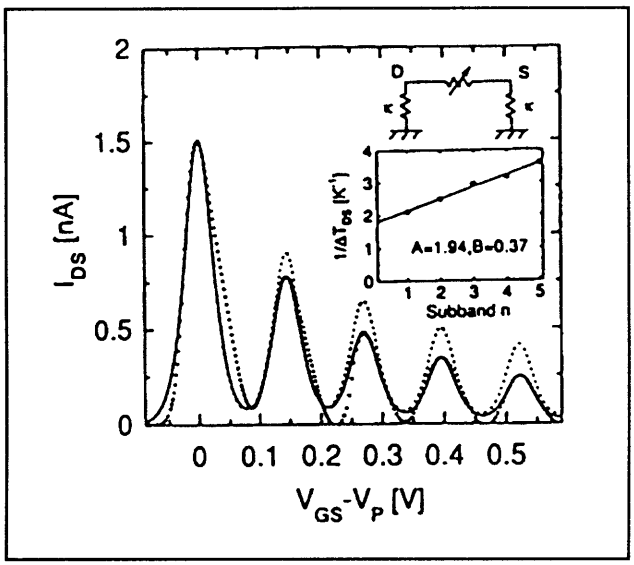

Figure 6. Radiation-induced thermal current versus gate voltage (•) shown together with calculated curves including the drain/source thermal conductance illustrated in the inset (____), and excluding that conductance (....). The inset shows the deduced temperature difference between the drain and source at different subband thresholds.

3.3.2 Direct Simulation of Photon-assisted Transport

Sponsor

National Science Foundation/MRSEC
Grant DMR 94-00334

Project Staff

Professor Qing Hu, in collaboration with .Kou Yakubo,[3] Shechao Feng[3]

We have proposed and theoretically investigated photon-assisted transport in quantum point contact devices. In essence, the process of photon-assisted transport is strictly analogous to the photoemission phenomenon in metals, which intrigued Einstein to propose the famous $E = \hbar\omega$ relationship. Following this analogy, we should expect an irradiated quantum point contact to exhibit photon-induced steps in the I_{DS} - V_{GS} curves, with the step width proportional to the photon energy. In spite of the intuitively plausible picture and the straightforward

[3] University of California at Los Angeles, Los Angeles, California.

analogy with the photoemission phenomenon, experimental investigations have failed to provide evidence for photon-assisted transport. We have carried out extensive measurements over a broad frequency range from 90 GHz to 2.5 THz (corresponding to $\hbar\omega$= 0.3 - 10 meV), with the radiation electric field polarization both along and perpendicular to the drain/source conductance path, which have yielded nothing but bolometric signals. It is natural to ask why such a simple process (which is analogous to so many well-established phenomena, such as photoemission in metals, photo-ionization of atoms, photon-excited bound-to-extended-state transitions in quantum-well structures, and photon-assisted tunneling in superconducting tunnel junctions) has not been observed in quantum-point-contact devices.

In this work, we solve time-dependent Schrödinger's equation numerically in order to investigate what conditions could produce a pronounced effect of photon-assisted transport. Our main finding is that the selection rule, which is the mathematical statement of the momentum conservation of the electron/photon systems, determines whether the electron transport is adiabatic or photon-excited. Mathematically, to achieve an appreciable photon-excited transition probability, the dipole-moment integration must be truncated to a region that is not much greater than the coherence length $1/\Delta k$, where Δk is equal to the momentum difference between the electrons before and after photon absorption/emission. This truncation can be achieved experimentally by either a localized electron state or a localized photon-field profile. Physically, this spatial localization of the electron or photon field provides the momentum spread that is necessary for the momentum conservation in the photon excitation process. Figure 7a shows a wave function (in k-space) in the presence of an ac field. The main peak at k = 0 corresponds to the wave function in a free space without radiation. The satellite peaks correspond to photon absorptions. Figure 7b shows the amplitudes of these peaks as functions of the ac-field spatial width. Clearly, photon-excitation process decreases dramatically as the ac-field spatial confinement loosens.

Our simulation study indicates that the selection rule requires a spatially confined ac field if the photon-excited transition is between two extended electronic states, such as the case for quantum-point-contact devices. This can be achieved by bringing the antenna terminals very close to the central region. Photon excitation can also be achieved by using double- or multiple-barrier structures to create quasibound electronic states. The spatially localized nature of these quasibound states provide the momentum change for the photon-assisted process. This understanding has been demonstrated experimentally in the observations of photon-assisted tunneling in quantum dots and photon-assisted transport in dual-gate devices.

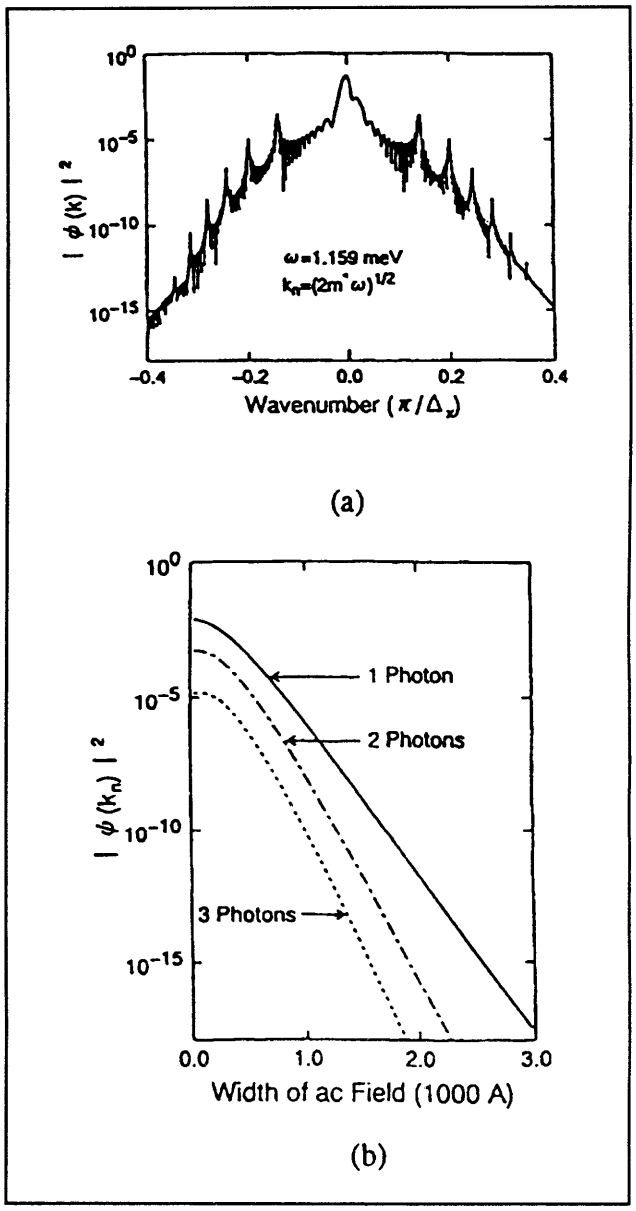

Figure 7. (a) Square of a wave function of free electrons (in k-space) under the irradiation of an ac field. The satellite peaks correspond to photon absorption (on the right of the main peak) and emission (on the left). (b) Values of photon-excited states as functions of the width of the ac field.

3.3.3 Photon-assisted Transport in Lateral Dual-gate Devices

Sponsors

MIT Lincoln Laboratory
Advanced Concept Program
Contract BX-5464
MIT Research Laboratory of Electronics
Postdoctoral Fellowship
National Science Foundation/MRSEC
Grant DMR 94-00334

Project Staff

Dr. Simon Verghese, Rolf A. Wyss, Dr. Thomas Schäpers

As our direct simulation study of photon-assisted transport indicates, photon absorption requires a momentum transfer of $\Delta k \sim m^* \omega/\hbar k_f$ for an electron of mass m^* with a wavevector $\sim k_f$ to absorb a photon with $k \sim 0$. This momentum transfer can be achieved either by localizing the photon field to within the coherence length $1/\Delta k$, or by localizing the electron wavefunctions. The devices described here supplies Δk by mainly localizing the electron wavefunction in one dimension that is parallel to the photon's polarization. Similar scheme has been successfully implemented in infrared ($\lambda \sim 10\mu m$) photon detectors using vertically grown quantum-well structures. These devices absorb photons when a 1D-localized electrons in a bound state is excited into the continuum. To maintain a steady-state operation, the depleted electrons in the quantum wells are supplied by thermionic electrons from the emitter over the barriers. In our case, the depleted electrons are supplied by tunneling injection from the source. Consequently, the eigenstates are quasibound states with lifetimes much greater than the modulation period of the ac field.

An SEM picture of an antenna-coupled dual-gate device is shown in figure 8, along with a side view of the device, a self-consistently calculated dc potential profile in the drain/source direction, and the transmission coefficient $T(\varepsilon)$ through such a structure. The peaks in the transmission coefficient correspond to the energy levels of the quasibound states, while the peak widths correspond to their lifetimes. In the presence of an ac field, photon-assisted transport (due to quasibound state to continuum transitions) can be modeled by an effective transmission coefficient $T\omega(\varepsilon)$, whose main peaks correspond to the original $T(\varepsilon)$ and the sidebands correspond to photon absorption or emission, as shown in figure 9a. Photon-induced current can be calculated in this model by taking the difference between the current calculated using $T_\omega(\varepsilon)$ and $T(\varepsilon)$.

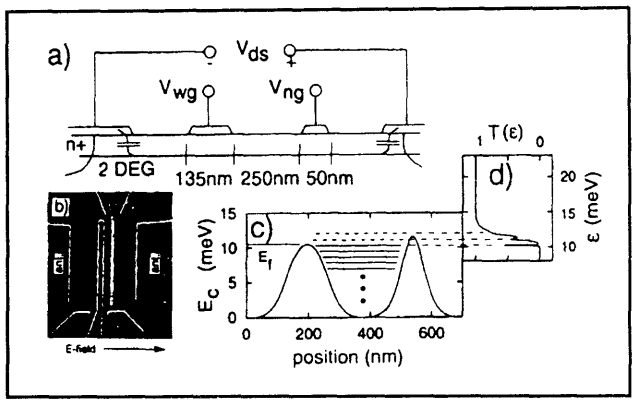

Figure 8. (a) Side view of a dual-gate device. (b) SEM picture of the device. (c) Self-consistently calculated dc potential profile for the device. (d) Transmission coefficient as a function of the energy.

Figures 9b and 9c show the measured radiation-induced current as functions of the drain/source bias voltage V_{ds} (curves labeled by i). The two sets of curves are taken with radiation frequencies at 90 GHz (in 9b) and 270 GHz (in 9c). The radiation power level at both frequencies is approximately the same. It is clear that the two sets of curves exhibit distinctively different features at the two radiation frequencies. The ones at 90 GHz show much sharper modulations of the radiation-induced current, while the ones at 270 GHz have much smoother features, which is due to the overlap of photon subbands at this high frequency, as illustrated in figure 9a. This frequency-dependent feature is the strongest evidence that the radiation-induced current is a photonic effect that depends on the energy of an individual photon. The curves labeled (ii) in figure 9b and 9c are calculated photocurrent based on the model of photon-assisted transport. They agree with the experimental results quite well. In comparison, the calculated radiation-induced current based on a bolometric model (labeled (iv) is frequency independent and cannot explain the experimental results taken at 270 GHz.

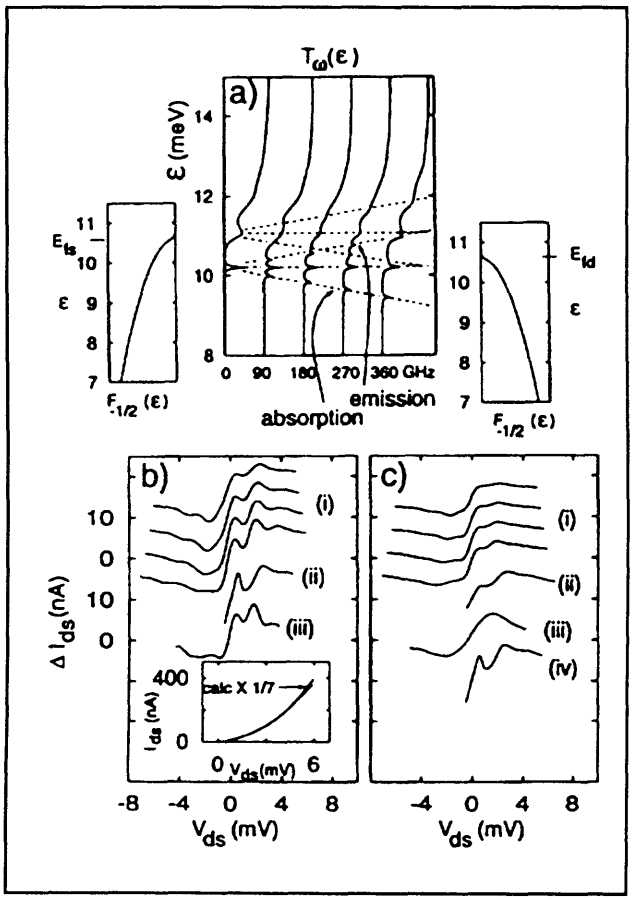

Figure 9. (a) Effective transmission coefficient that includes the effect of photon absorptions and emissions. (b) and (c) Curves (i): measured radiation-induced current at 90 GHz (b) and 270 GHz (c). Curves (ii): calculated radiation-induced current based on the model of photon-assisted transport. Curve (iv): calculated radiation-induced current based on heating model.

3.3.4 Subpicosecond Dynamical Studies of Quantum-effect Devices

Sponsors

MIT Lincoln Laboratory
Advanced Concept Program
Contract BX-5464
National Science Foundation/MRSEC
Grant DMR 94-00334

Project Staff

Dr. Simon Verghese, Noah D. Zamdmer, Professor Qing Hu, in collaboration with Dr. Elliot Brown,[4] Dr. Michael R. Melloch[5]

The modern solid-state physics and electrical engineering communities are witnessing a trend where electronic devices are becoming smaller and speeds are becoming faster. This is driven by modern society's insatiable appetite for the increased capacity of information processing and transmission. As a result, the smallest feature size of state-of-the-art devices has reached several hundred angstroms. At this length scale, the intersubband spacing and the Coulomb interaction energy are in the millielectrovolt range, corresponding to THz frequencies. In a related project (see previous sections), we have studied transport properties of antenna-coupled quantum-effect devices under coherent far-infrared radiation whose frequencies are comparable to the intersubband spacing. In this project, we are carrying out transport studies in time domain by using subpicosecond electrical pulses generated by Auston switches to study the dynamical processes of electrons in quantum-effect structures.

Although our work in frequency domain has yielded new information about quantum-effect devices, a complementary approach is to study the response of the quantum devices in time-resolved fashion by using a pump-and-probe method with a pulsed laser. A 100-fs laser pulse contains frequency components up to 10 THz, which should enable us to perform spectroscopic studies on quantum devices over a broad frequency range that covers all the interesting energy levels, namely the intersubband transition and Coulomb interaction energies. Furthermore (and perhaps the most attractive feature of the time-domain studies), the time-resolved studies can reveal information that frequency-domain studies cannot reveal, namely the time scale of transport process in quantum devices. This is one of the basic issues in determining the potential applications of the quantum devices.

We are pursuing two types of measurements in this project. The first one involves a far-infrared spectrometer pumped by a mode-locked Ti:Sapphire laser which we have constructed recently, as shown in figure 10. In this set up, two antenna-coupled Auston switches are pumped by a Ti:Al_2O_3 pulsed laser. The THz electrical pulses are

[4] MIT Lincoln Laboratory, Lexington, Massachusetts.

[5] Purdue University, West Lafayette, Indiana.

launched into free space and then combined by a beam splitter. The combined beam is a superposition of two coherent subpicosecond electrical pulses whose relative time delay can be varied. These combined pulses will then be focused onto an antenna-coupled quantum device and generate a dc electrical current in the device through the photon-assisted transport/tunneling process. Effectively, the generated electrical current is proportional to the time autocorrelation function of the whole system, whose Fourier transform will give the frequency response of the system. This measurement is essentially the same as that using a conventional far-infrared Fourier transform spectrometer (FTS), which uses a Hg-arc lamp as its source. There are several major advantages of the pulsed laser system, however. First, its source is much brighter than that of the FTS so that far-infrared nonlinear spectroscopy can be performed. Second, the short duration of the laser pulses minimizes the heating effect and thus enhances the relative strength of the photon-assisted quantum process.

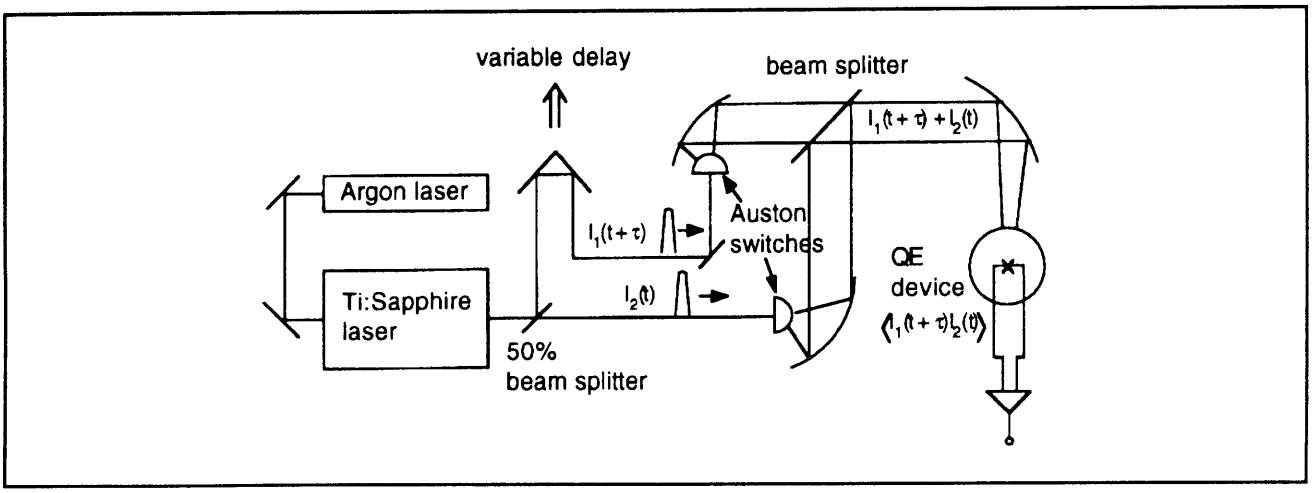

Figure 10. Schematic of an interferometer pumped by a pulsed Ti:Sapphire laser.

The second type of experiment involves a pump-and-probe method, by integrating two Auston switches monolithically with the quantum-effect devices, as shown in figure 11. One switch will be used to apply a short electric pulse on the input, and the second one will be used to probe the output electrical current in a time-resolved fashion. This scheme differs from the first one in that the pump and probe beams are focused on different spots. In this way, we can measure the time scale of the transport process from the input to the output, as well as the spectroscopic information of the system. In order to achieve a high speed from the Auston switches, lattice-matched low-temperature-grown (LTG) GaAs materials will be used which have subpicosecond recombination time.

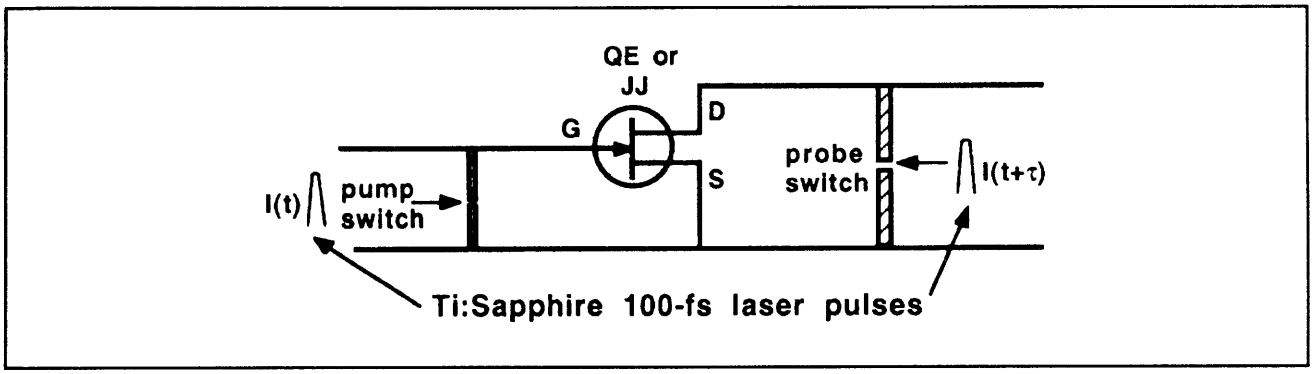

Figure 11. Schematic of a three-terminal (QE or Josephson) device pumped by a subpicosecond electrical pulse at the input, and the induced output current can be time-resolved by another time-delayed probe beam.

3.4 Intersubband Transitions in Coupled Double Quantum-well (DQW) Structures

Coupled DQWs are simply voltage tunable two-level or multi-level systems. Therefore, under specific bias conditions for carefully designed and fabricated DQWs, the devices can generate far-infrared radiation (when the initial state is higher than the final state), detect far-infrared radiation (when the initial state is lower than the final state), or perform nonlinear optical functions such as parametric amplifications.

3.4.1 Far-infrared Lasers and Detectors Using DQW Structures

Sponsors

Rome Air Force Laboratory
Graduate Fellowship
U.S. Army Research Office
Grant DAAL03-92-G-0251

Project Staff

James Ernstmeyer, Bin Xu, Jurgen H. Smet, Professor Qing Hu, in collaboration with Dr. Michael R. Melloch[6]

The schematic of a single DQW structure is shown in figure 12a. The conduction band profile, subband structures, and carrier densities are calculated self-consistently from Schrödinger and Poisson equations, after typical five iterations. Figure 12b shows the transmission coefficient through such a structure, whose peaks correspond to the subband levels in (a). Clearly, the intersubband energy difference $E_2 - E_1$ (corresponding to the radiation frequency) can be tuned by a bias voltage between the emitter and collector. The most important parameter that determines the radiation properties (due to the $1 \rightarrow 2$ intersubband transition) of this DQW structure is the dipole moment $<1|z|2>$, or equivalently, the oscillator strength f_{12}, which is the ratio of the quantum mechanical radiative decay rate over that of a classical Hertzian dipole at the same frequency.

By using a tight-binding model to calculate the eigenenergy levels of the coupled DQW device, we can obtain the expression for the energy of the two lowest levels,

$$E_{2,1} = E_o \pm \sqrt{(\Delta_o/2)^2 + (eV/2)^2},$$

where the field-induced energy splitting $\Delta = |E_2 - E_1| = \sqrt{(\Delta_o)^2 + (eV)^2}$. Δ as a function of the bias voltage V is shown in figure 13. The energy splitting takes the minimum value Δ_o at the anti-crossing point, above which the energy of the state that is mainly localized in the left well becomes higher than that of the state that is mainly localized in the right well. Since the state mainly localized in the left well couples strongly to the emitter (which always has a higher Fermi energy than the collector), and is therefore the initial state that is filled with electrons, figure 13 indicates that the relative energy difference between the initial and final states (not only the amplitude but also the sign) can be tuned by the bias voltage. Consequently, the same DQW structure can be used as both a detector and an emitter. As a detector, the initial state lies below the final one; while as an emitter, the initial state lies above the final one.

[6] Purdue University, West Lafayett, Indiana.

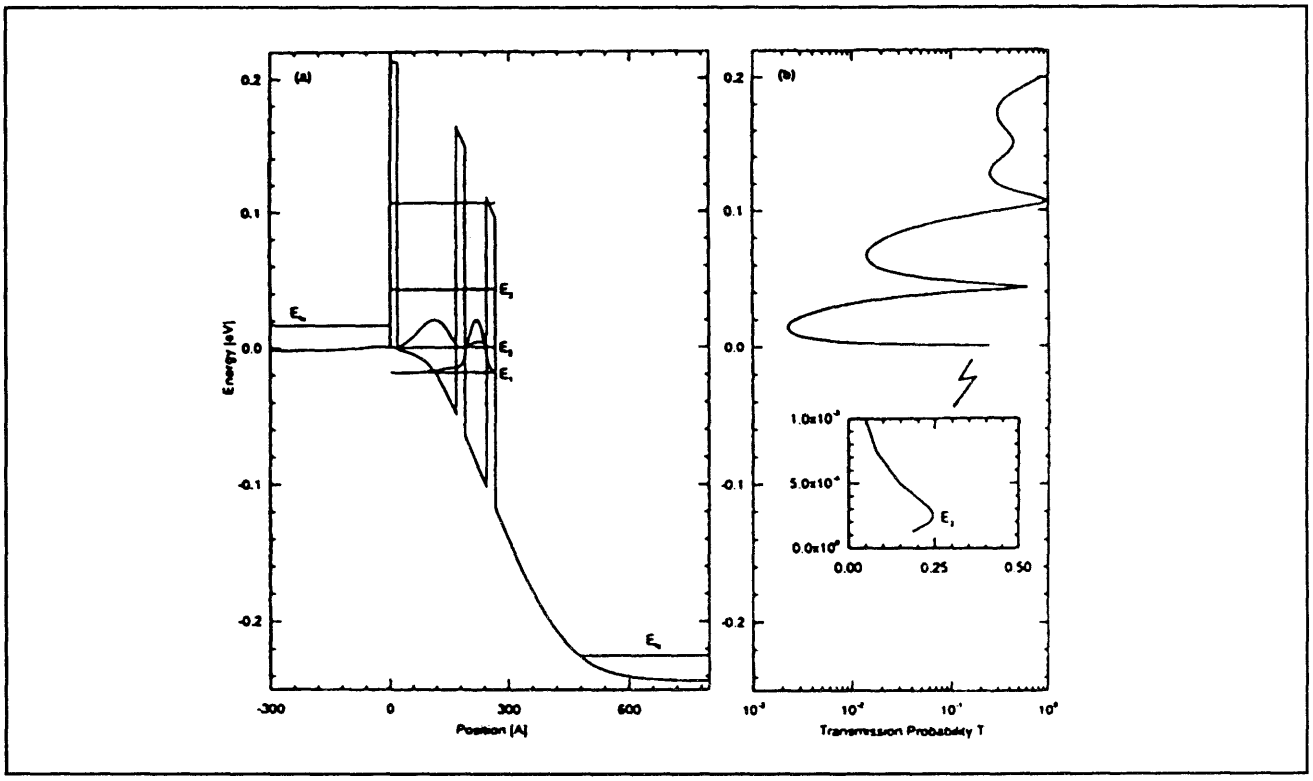

Figure 12. (a) Conduction band profile and the square of wavefunctions at a bias voltage of 240 mV for a typical DQW structure. The wider emitter well (on the left) is to ensure that a large carrier density can be achieved at a desired intersubband spacing $E_2 - E_1$. (b) Transmission coefficient T(E) as a function of the electron incident energy. The peak positions in T(E) correspond to the subband levels in (a). The resonance widths in T(E) determine the escape lifetimes.

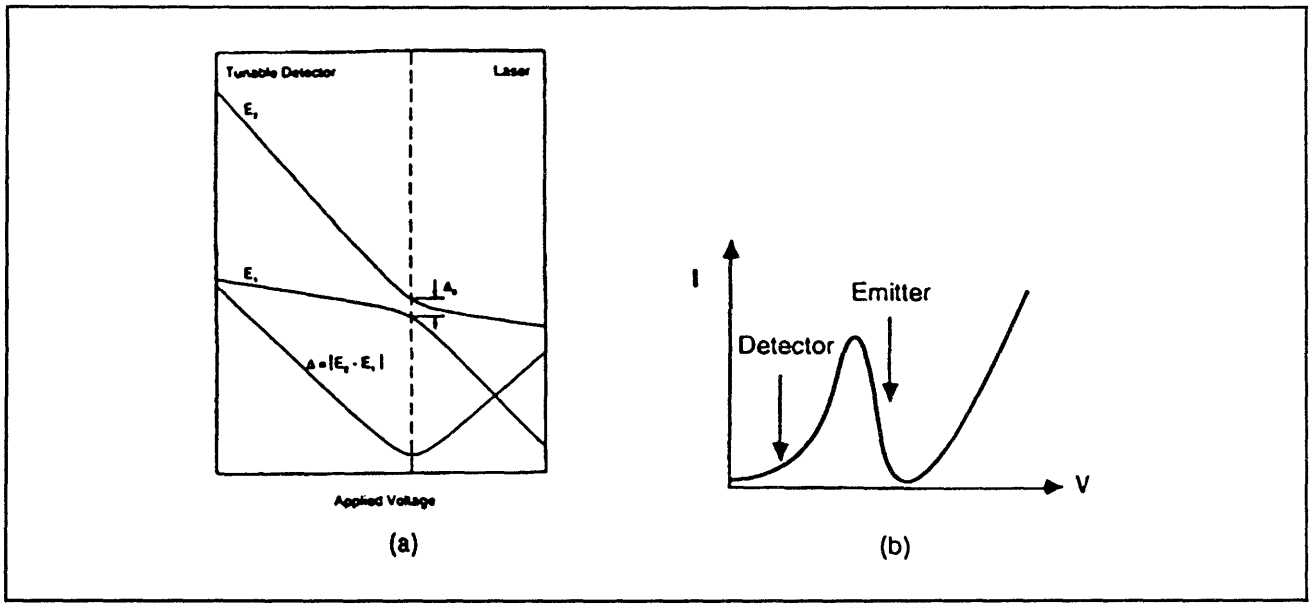

Figure 13. Left: Energy level diagram as a function of applied voltage, which exhibits an anticrossing with a gap Δ_0. At low voltages the device can be used as a tunable detector, as indicated in the figure on the right, and beyond the anticrossing it functions as a field-tunable emitter.

We have performed a thorough analysis on the radiation properties of the coupled DQW structures. In figure 14, the oscillator strength, which is mainly determined by the dipole moment between the two states, is plotted as a function of the photon energy. Clearly, for experimentally achievable values of the anticrossing gap, for example, $\Delta_0 = 4$ meV (corresponding to a 20-Å thick $Al_{0.24}Ga_{0.76}As$ middle barrier in the GaAs/AlGaAs DQW structures), the oscillator strength is close to 0.2, making the DQW an efficient radiator. Using the free-carrier plasmas in a heavily doped emitter and collector for mode confinement, we have calculated the required inverted population density Δn at the lasing threshold, which are plotted in figure 14 for different values of Δ_0. It appears that $\Delta n \sim 10^{13}/cm^2$ in the THz frequency range for $\Delta_0 = 4meV$. But using many identical DQW modules connected in series, we can reduce this threshold density by a factor of N, which is the number of modules. Using 100 DQW modules, the threshold carrier density will be approximately $10^{11}/cm^2$. At this density, the dominating nonradiative relaxation mechanism is electron-electron scattering, which is estimated to have a relaxation time on the order of 20 picoseconds. Consequently, lasing threshold can be reached at $e\Delta n/\tau \sim 1kA/cm^2$ current density, which is quite feasible.

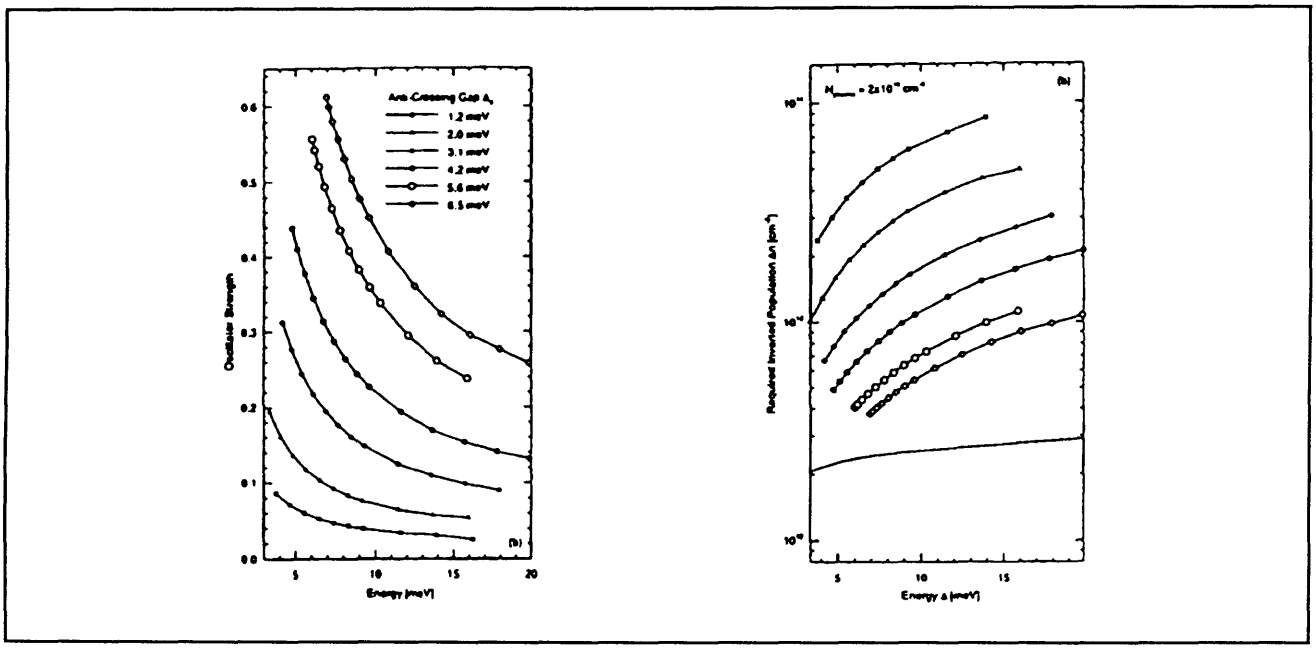

Figure 14. Left: Oscillator strengths for the intersubband transition as a function of the photon energy and with the anticrossing gap as a parameter. Right: Threshold inverted population density required to overcome plasma confinement losses.

3.4.2 Magnetotunneling Spectroscopy of DQW Structures

Sponsor

U.S. Army Research Office
Grant DAAL03-92-G-0251

Project Staff

Jurgen H. Smet, Professor Qing Hu, in collaboration with Professor Clifton G. Fonstad, Jr.

One of the major difficulties in achieving far-infrared lasing in DQW devices is the fast nonradiative relaxation rate (~ 20 picosecond) compared to the slow radiative relaxation process (~ 1 microsecond). The nonradiative relaxation processes are so fast because the subbands in a quantum well have continuum states for all the possible transverse momentum values (perpendicular to the growth direction), instead of discrete energy levels. Thus, the conservation of energy and transverse momentum can be simultaneously satisfied for these processes. Similar to the concept employed to confine plasmas in a tokamak, several groups have proposed the use of magnetic fields to reduce the dimensionality of the electron system in order to suppress nonradiative relaxation processes. Under a strong field along the growth direction, the transverse motion of electrons will be confined in cyclotron orbits and their energy spectrum will be quantized at Landau levels. This magnetic field-induced transverse confinement, along with the longitudinal confinement provided by the quantum-well structures, will effectively reduce the dimensionality

of the electron system to that of a zero-dimensional system, similar to that of quantum-dot systems. Consequently, the detrimental nonradiative relaxation processes will be significantly reduced. In this scheme, the applied longitudinal magnetic field will not affect transport in that direction or the dipole moment associated with the transition between two subbands. Therefore, the field will not have any adverse effect on the radiative process, and thus will substantially increase the radiation efficiency $\eta = \tau_{nonrd}/\tau_{spon}$.

Motivated by the magnetic suppression effect, we have performed extensive tunneling studies of DQWs in strong magnetic fields with both a longitudinal and transverse component. This study, called *magnetotunneling spectroscopy,* is a very powerful spectroscopic tool to measure the subband levels and in-plane energy-momentum dispersion (crucial information for any intersubband devices) with much greater accuracy than a dc tunneling study alone would yield. In the previous report, we have shown current oscillations as a function of a longitudinal magnetic field. This magnetooscillation is analogous to de Haas-Shubinikov oscillation, whose period in 1/B gives accurate measurements of the intersubband energy levels. In this work, we have extended the magnetotunneling spectroscopy to include a transverse magnetic field.

Under a transverse or in-plane magnetic field (with the field perpendicular to the current-flow direction), as well as a longitudinal one, electrons will acquire momentum in the transverse direction while traversing the MQW structures. Thus, the conservation of transverse momentum is no longer valid. Consequently, the applied transverse field broadens the resonant peaks in the tunneling I-V characteristics, and shifts the position of the resonances to higher bias voltage, as shown in figure 15.

Using this method, we can perform spectroscopy in the I-V curve region, where it has a negative dynamic resistance (NDR) that otherwise would be inaccessible, due to the instability associated with the NDR. This information is crucial for laser operations, since the NDR region corresponds to the initial state with a higher energy than the final state, which is the normal operating condition for lasers. figure 16 shows the I-V curve and the energy levels of a DQW device measured from magnetotunneling spectroscopy. The energy levels in the NDR region (represented by the open circles) are measured with an in-plane magnetic field applied.

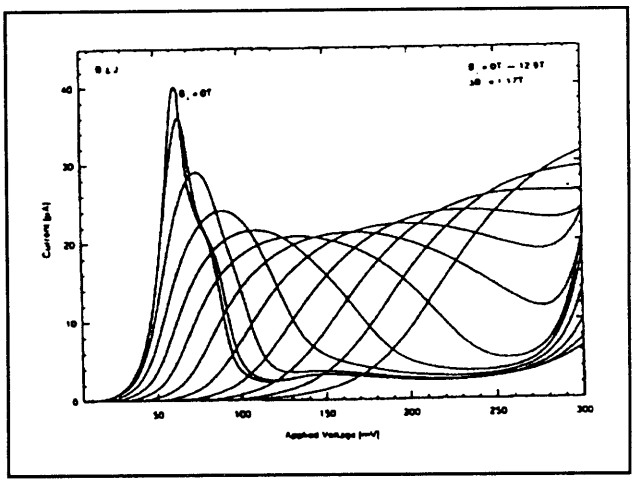

Figure 15. I-V tunneling characteristics near resonance of a DQW device with an in-plane field varying from 0 T to 12.9 T in steps of 1.17 T.

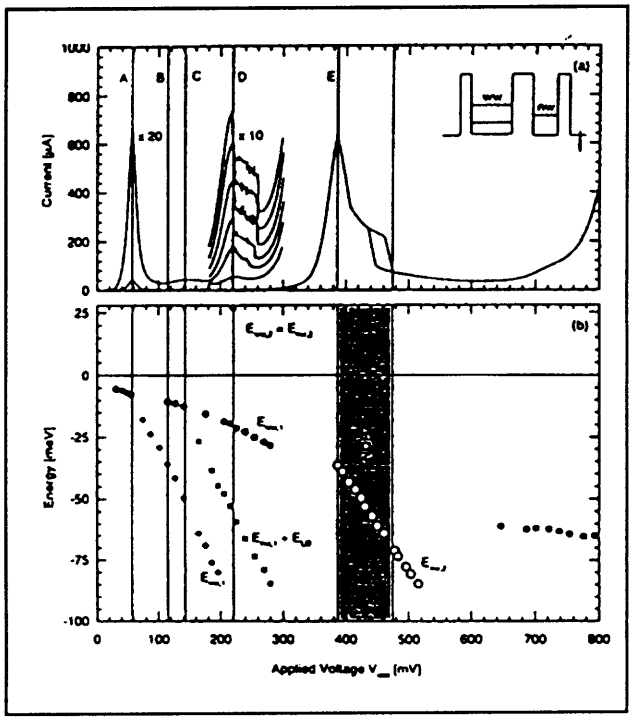

Figure 16. (a)I-V characteristic and (b) the subband energies as functions of the bias voltage at 4.2 K. The quasi-Fermi level in the emitter well is used as the energy reference (i.e., $E_{FE} = 0$). The open-circle data in the negative dynamic region (NDR) was obtained by applying an in-plane field to broaden the resonance peak.

3.4.3 Far-infrared Optical Parametric Amplifiers Using DQWs

Sponsors

Hertz Foundation Fellowship
U.S. Army Research Office/ASSERT
Grant DAAH04-94-G-0167

Project Staff

Ilya Lyubomirsky, Professor Qing Hu, in collaboration with Dr. Michael R. Melloch[7]

It is well known in the field of nonlinear optics that the nonlinear susceptibility $\chi^{(2)}$ is large near a resonant frequency for a system that is lack of inversion symmetry. Such a large $\chi^{(2)}$ has been widely used in second harmonic generation, second frequency generation, and parametric amplification at optical and near-infrared frequencies, where coherent sources at pump frequencies are available. As far as its optical properties are concerned, a quantum-well device acts like a giant atom, whose resonant frequencies are in the mid- to far-infrared frequencies. Naturally, if we design a QW structure such that it has resonances at mid-infrared frequency ($\lambda \sim 10$ microns) and far-infrared frequencies, we can use widely available CO_2 lasers as a pump source to parametrically generate far-infrared radiations. This nonlinear photon conversion process is illustrated in figure 17a.

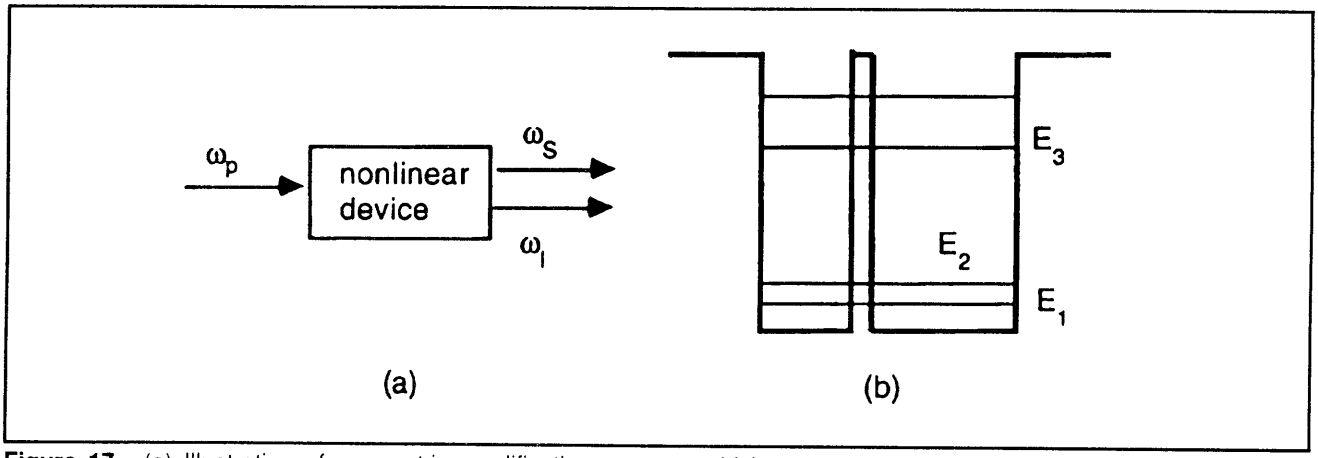

Figure 17. (a) Illustration of parametric amplification process, which converts a photon with a frequency ω_P into two photons with frequencies ω_I and ω_S, with $\omega_I + \omega_S = \omega_P$; (b) An asymmetric DQW structure that could produce a large $\chi^{(2)}$ at mid- and far-infrared frequencies.

However, a single quantum well has inversion symmetry, and therefore has a vanishing $\chi^{(2)}$. This problem can be solved easily by using a coupled DQW structure with an asymmetric well widths, as shown in figure 17b. In this structure, the energy differences between level 3 and level 1 and 2 are close to 120 meV (corresponding to a wavelength of 10 microns). These intersubband transition energies correspond to the pump and idler frequencies. The energy difference between level 1 and 2 is approximately 10 meV, corresponding to the far-infrared signal frequency. The nonlinear susceptibility $\chi^{(2)}$ is proportional to the product of three dipole moments, $\langle z_{12}\rangle\langle z_{13}\rangle\langle z_{23}\rangle$. By careful designing, each dipole moment can be as large as several 10 Å, which is at least one order of magnitude larger than that for optical transitions in atomic systems. Using the doubly resonant structure shown in figure 17b, we estimate $\chi^{(2)}$ to be as large as 10^{-6}m/V, which is four orders of magnitude larger than the value for bulk GaAs materials. This extraordinarily large $\chi^{(2)}$ can be used for efficient parametric amplifications. The challenging issue of phase-matching can be solved by using Stark effect (changing the resonant conditions by applying a bias voltage) to diminish $\chi^{(2)}$ beyond the coherence length.

[7] Purdue University, West Lafayette, Indiana.

3.4.4 Millimeter-wave, THz, and Subpicosecond Facilities

Professor Hu's laboratory is equipped with various millimeter-wave and infrared sources which can generate coherent and incoherent radiation from 75 GHz up to 30 THz. These include: Gunn oscillators at W-band frequencies (75-11 GHz); a frequency doubler, tripler, and quadrupler using Schottky diodes at 200, 300, and 400 GHz; an optically pumped far-infrared laser which generates coherent radiation from 245 GHz to 8 THz; and an infrared Fourier transform spectrometer which is capable in performing linear spectroscopy from 45 GHz to 30 THz and beyond. This laboratory is also equipped with various cryogenic millimeter-wave and infrared detectors. These include: Si composite bolometers InSb hot-electron bolometers, SIS (superconductor-insulator-superconductor) receivers, and high Tc Josephson detectors. Recently, with the support from AT&T, a mode-locked Ti:sapphire laser that can generate optical pulses as short as 70 femtosecond was purchased and installed.

3.5 Publications

3.5.1 Journal Articles

de Lange, G., B.R. Jacobson, and Q. Hu. "Micromachined Millimeter-wave SIS Mixers." *IEEE Trans. Appl. Supercond.* Forthcoming.

Gupta, R., Q. Hu, D. Terpstra, G.J. Gerritsma, and H. Rogalla. "A Noise Study of a High-Tc Josephson Junction under Near-millimeter-wave Irradiation." *Appl. Phys. Lett.* 64: 927 (1994).

Hu, Q., R.A. Wyss, C.C. Eugster, J.A. del Alamo, and S. Feng. "Far-infrared Study of an Antenna-coupled Quantum Point Contact." In *Quantum Well Intersubband Transition Physics and Devices.* Eds. H.C. Liu, B.F. Levine, and J.Y. Andersson. Boston: Kluwer Academic, 1994, p. 553.

Smet, J.H., C.G. Fonstad, and Q. Hu. "Intrawell and Interwell Intersubband Transitions in Multiple Quantum Wells." Submitted to *J. Appl. Phys.*

Smet, J. H., C.G. Fonstad, and Q. Hu. "Magnetotunneling Spectroscopy with both In-plane and Longitudinal Fields." Submitted to *Phys. Rev. B.*

Verghese, S., R.A. Wyss, T. Schäpers, A. Förster, M.J. Rooks, and Q. Hu. "Photon-assisted Transport through Quantized Energy States in a Lateral Dual-Gate Device." Submitted to *Phys. Rev. Lett.*

Wyss, R.A., C.C. Eugster, J.A. del Alamo, Q. Hu, M.J. Rooks, and M.R. Melloch. "Far-infrared Radiation-induced Thermopower in a Quantum Point Contact." *Appl. Phys. Lett.* 66: 1144 (1995).

Yakubo, K., S. Feng, and Q. Hu. "Direct Simulation of Photon-assisted Quantum Transport." Submitted to *Phys. Rev. B*

3.5.2 Conference Presentations

de Lange, G., B.R. Jacobson, and Q. Hu. "Micromachined Millimeter-wave SIS Mixers." Presented at 1994 Applied Superconductivity Conference, Boston, Massachusetts, 1994.

Hu, Q., J.H. Smet, and C.G. Fonstad. "Terahertz Lasers Using Quantum-well Structures." Presented at the SPIE International Symposium, OE/LASE '94, Los Angeles, January 25, 1994. (invited)

Hu, Q., R. Gupta, D. Terpstra, G.J. Gerritsma, and H. Rogalla. "Response of High-Tc Ramp-type Josephson Junctions to Near-millimeter-wave Radiation." Presented at the SPIE International Symposium, OE/LASE '94, Los Angeles, January 26, 1994. (invited)

Schäpers, T., R.A. Wyss, Q. Hu, M. Krueger, A. Föster, A. van der Heart, and H. Lueth. "Far-infrared Studies of Planar Resonant Tunneling Field Effect Transistors." Presented at the American Physical Society Meeting, Pittsburgh, Pennsylvania, 1994; *Bull. Amer. Phys. Soc.* 39: 352 (1994).

Verghese, S., R.A. Wyss, T. Schäpers, Q. Hu, E.R. Brown, K.A. Mcintosh, and M.R. Melloch. "Broad-band Far-infrared Spectroscopy of Mesoscopic Devices." Presented at the American Physical Society Meeting, Pittsburgh, Pennsylvania, 1994; *Bull. Amer. Phys. Soc.* 39: 352 (1994).

Wyss, R.A., C.C. Eugster, J. del Alamo, Q. Hu, M.J. Rooks, and M.R. Melloch. "Far-infrared Radiation-induced Thermopower in an Antenna-coupled Quantum Point Contact." Presented at the American Physical Society Meeting, Pittsburgh, Pennsylvania, 1994; *Bull. Amer. Phys. Soc.* 39: 352 (1994).

3.5.3 Theses

Jacobson, B.R. *A Micromachined SIS Mixer.* S.M. thesis. Dept. of Electr. Eng. and Comput. Sci., MIT, 1994.

Smet, J.H. *Intrawell and Interwell Intersubband Transitions in Single and Multiple Quantum Well Heterostructures.* Ph.D. diss. Dept. of Electr. Eng. and Comput. Sci., MIT, 1994.